Ocean Engineering 266 (2022) 112739

Contents lists available at ScienceDirect

Ocean Engineering

journal homepage: www.elsevier.com/locate/oceaneng

Elastomeric sandpaper *replicas* as model systems for investigating elasticity, roughness and associated drag in a marine biofilm flow cell

Alexandra Snowdon [a,*], Shi-Qi An [b], Alistair Finnie [c], Marie Dale [c], Simon Dennington [a], Jennifer Longyear [c], Julian Wharton [a], Paul Stoodley [a,b,d]

[a] National Centre for Advanced Tribology, Faculty of Engineering and Physical Sciences, Southampton University, United Kingdom
[b] National Biofilm Innovations Centre, School of Biological Sciences, Southampton University, United Kingdom
[c] AkzoNobel/International Paint Ltd., Stoneygate Lane, Gateshead, United Kingdom
[d] Departments of Microbial Infection and Immunity and Orthopaedics, The Ohio State University, OH, Columbus, USA

ARTICLE INFO

Keywords:
Physico-mechanical
Elasticity
Roughness
Drag
Flow cell
Biofilm model

ABSTRACT

Biofilm heterogeneity and adaptability complicates efforts to link biofilm structural and mechanical properties to frictional drag. As a result, rigid structures are typically used as the benchmark for studying biofilm-associated drag. Elastomeric sandpaper replicas were generated to be used as model systems for investigating the effect of roughness and elasticity on drag, over the Reynolds number range of approximately 2.0×10^4 to 5.2×10^4 Re using a marine biofilm flow cell. To control for roughness parameters and surface topography the replicas were created for sandpaper grit numbers: P40, P80 and P240 with average measured roughness (S_a) of 108, 49 and 16 μm, respectively. Profilometry confirmed that there was no significant difference between the roughness of the rigid sandpaper sources and the material replicas. The marine biofilm flow cell was fitted with a clear lid, which allowed real-time visualisation of the replicas' surface topography using Optical Coherence Tomography. Pressure drop measurements, expressed as a friction coefficient, revealed that the elastomeric sandpaper replicas had a significantly higher associated drag, of up to 52%, when compared to the rigid counterparts. From statistical analysis it was confirmed that material mechanical properties, such as elasticity, and surface roughness both significantly affect drag. Elastic model systems can be used to enhance our understanding of biofilm physico-mechanics and their role in marine drag.

1. Introduction

Biofilms are composed of a community of sessile microorganisms embedded within a viscous exudate (the matrix). The matrix is dominated by extracellular polymeric substances (EPS) (Di Martino, 2018; Flemming and Wingender, 2010) and water (Berlanga and Guerrero, 2016), and offers protection to microbial cells from external stressors, such as environmental, chemical or mechanical factors (Peterson et al., 2013).

In the shipping industry, the presence of biofilms on ship hulls can increase frictional drag which has significant economic and environmental consequences, such as higher fuel consumption and correspondingly greater greenhouse gas emissions (Townsin, 2003). An increase in ship shaft power between 1% and 18% due to the presence of a biofilm is a frequently cited figure in the current literature (Haslbeck and Bohlander, 1992; Schultz et al., 2011; Yeginbayeva et al., 2020). Due to the complexity of measuring drag at ship-scale, the majority of marine biofilm drag studies are executed at a laboratory scale, for example using flow cells on the order of 1 m; results can then be extrapolated to predict ship-scale drag (Schultz et al., 2015; Yeginbayeva et al., 2020). Importantly, care must be taken when extrapolating data to ship-scale as ship relevant Re are typically orders of magnitude higher than the Re range covered using smaller flow cells (Fabbri et al., 2019). Operating at a smaller scale is useful for screening since more replicates can be ran providing greater rigor; further, environmental conditions can be controlled, and physico-mechanical properties can be studied more closely (Fabbri et al., 2018). It is known that biofilm morphological properties, such as surface roughness (Andrewartha et al., 2010; Li et al., 2019), and physico-mechanical (combined

* Corresponding author.
E-mail addresses: A.Jackson@soton.ac.uk (A. Snowdon), s-q.an@soton.ac.uk (S.-Q. An), alistair.finnie@akzonobel.com (A. Finnie), marie.dale@akzonobel.com (M. Dale), s.p.dennington@soton.ac.uk (S. Dennington), jennifer.longyear@akzonobel.com (J. Longyear), j.a.wharton@soton.ac.uk (J. Wharton), p.stoodley@soton.ac.uk (P. Stoodley).

https://doi.org/10.1016/j.oceaneng.2022.112739
Received 28 March 2022; Received in revised form 5 July 2022; Accepted 24 September 2022
Available online 8 October 2022

Abbreviations

EPS	extracellular polymeric substances
DIC	digital image correlation
OCA	optical contact angle
OCT	optical coherence tomography
PDMS	polydimethylsiloxane
PIV	particle image velocimetry
PTFE	polytetrafluoroethylene
PVC	polyvinyl chloride

physical and mechanical) properties are significant in influencing drag (Schultz et al., 2015; Watanabe, 1969); yet, the relative contribution of these properties is poorly understood (Blauert et al., 2015; Hartenberger et al., 2020; Picioreanu et al., 2018). In part, this is attributed to the high level of heterogeneity and adaptability that biofilms exhibit, which leads to wide variations in efforts to relate biofilm characteristics to drag (Schultz and Swain, 2000).

To study biofilm-associated drag, experimental and computational models have been adopted which use homogenous and rigid structures to mimic biofilm behaviour (Hartenberger et al., 2020; Yusim and Utama, 2017). A benefit of utilising a synthetic system as a biofilm substitute is that the material has reproducible properties that can be controlled, which is a challenge when using natural biofilms. Rigid and homogenous structures, such as embedded sand grains or sandpaper, can approximate average biofilm roughness profiles and have been reported to cause similar, if not equivalent, drag to biofilms under specified experimental conditions (Hartenberger et al., 2020; Murphy et al., 2018). However, in many other studies, drag associated with biofilms greatly exceeds that which would be anticipated for a rigid equivalent (Hartenberger et al., 2020; Picologlou et al., 1980).

Biofilms are viscoelastic materials, which typically exhibit a time-dependent response when under applied stress, such as hydrodynamic shear (Gloag et al., 2018; Shaw et al., 2004). The deformation behaviour of viscoelastic materials, for example wide-ranging lab and environmental biofilms, has been repeatedly captured using mechanical methods, such as rheology, indentation (Peterson et al., 2013; Stoodley et al., 1999) and imaging methods (Blauert et al., 2015; Depetris et al., 2019; Picioreanu et al., 2018). Biofilm material properties have long been hypothesised as a major reason for why biofilm fouling causes high frictional drag (Picologlou et al., 1980; Schultz and Swain, 2000). Therefore, whilst conventional methods used to physically model biofilms involve implementing rigid materials of different roughness', they generally do not account for viscoelastic physico-mechanical properties, which could alter fluid-structure interactions and possibly lead to the mis-estimation of drag (Hartenberger et al., 2020; Picioreanu et al., 2018; Picologlou et al., 1980).

To investigate differences in drag associated with a rigid and deformable material, Lewkowicz and Das (1986) introduced a compliant drag-production mechanism into a biofilm-associated drag model using nylon tufts. They revealed a significant increase in drag when comparing the drag induced by the compliant system to the rigid controls, which was explained by fluid-structure interactions caused by the surface protrusions. Andrewartha et al. (2010) adopted a similar approach using woollen strands. The drawback of these models is that although artificial protrusions are individual free moving structures the mechanical properties and the roughness patterns cannot be varied independently as they could be with synthetic material models.

Alternatively, artificial biofilms which involve embedding bacterial cells in a hydrogel (Körstgens et al., 2001; Strathmann et al., 2000), have been implemented as models for studying biofilm mechanics and deformation behaviour as they can mimic biofilm-like responses to shear (Di Martino, 2018; Stewart et al., 2015). Yet, Kandemir et al. (2018) found that under specified conditions there was no difference observed between a hydrogel with and without embedded bacteria. A benefit of a model with no living component is that natural variability as well as structural and biological complexity observed in biofilms is removed (Macedo et al., 2014). Moreover, a synthetic material can be manipulated to simulate an array of physico-mechanical characteristics. El-Labbad (1987) utilised smooth panels of agar gels of different concentrations to mimic different levels of biofilm 'slime': 0.5% was used to represent light to moderate slime and 1% was implemented for heavy slime. The denser slime equivalent (1% agar) caused a greater increase in drag (El-Labbad, 1987), which suggests that differences in drag between the agar gels were driven by material mechanical properties.

Due to the species and mechanical property diversity of biofilms there is no doubt that some can be characterised as rigid and rough, much like sandpaper structures, or even uniform with repeating units (Wagner et al., 2010) – yet this is likely the exception as opposed to the rule. The aim of this study is to build upon and extend rigid conventional methods by introducing a tailored elastic component. The objective of the present work is to determine the relative contribution of elasticity and roughness to drag using elastomeric and rigid *replicas* of the surfaces of sandpapers of various roughness grades. Although biofilms are spatially heterogenous, a defined and repeatable surface profile was incorporated into the *replicas* to simplify the system and to allow physico-mechanical properties to be the focus of the study. Drag was measured using pressure drop sensors installed into a flow cell and was expressed as a Fanning friction factor (C_f) (Fabbri et al., 2019; Li et al., 2019). It was hypothesised that the elastomeric structures would induce a significantly greater drag than rigid structures of comparable roughness. Topographical change in response to hydrodynamic shear was simultaneously measured using Optical Coherence Tomography (OCT), a non-invasive imaging technique that has been previously implemented for studying biofilm mechanics at the meso-scale (Blauert et al., 2015; Wagner et al., 2010; Wagner and Horn, 2017). By utilising a fully synthetic tailored system, such as the one proposed in the present study, the effects of surface geometry and mechanical properties on drag can be studied in isolation. If we can determine under which conditions physical and/or mechanical properties are most influential to drag then better insights into the efficiency of coating technologies for the prevention and management of biofilms can be gained (Fabbri et al., 2018, 2019; Hartenberger, 2019). These findings will help advance the development of a more accurate experimental marine biofilm models and can be used to further study the contribution of physico-mechanical properties on biofilm-associated drag.

2. Material and methods

2.1. Cast and replica preparation

The casting and moulding process involved three groups of materials, referred to as *source*, *intermediate*, and *replica* (Table S1). Two *sources* (either sandpaper or smooth PVC) were used to create an impression in the *intermediate* material to produce a negative mould (Fig. 1c). Materials (elastomeric or rigid when set) were then poured into the *intermediate* moulds to generate *replicas* of the *source* materials (Fig. 1f). The *replicas* were generated to be compatible with the flow cell and measured 85 cm × 5.5 cm. Between all steps (Fig. 1) polytetrafluoroethylene (PTFE) release spray was used to ensure easy removal from surfaces.

2.1.1. Source materials

Replicas were generated from two *source* materials: sandpaper (3M, Bracknell, UK) and polyvinyl chloride (PVC) panels (Chemical Process Solutions, Seaham, UK). Sandpaper of three different grit numbers: P40, P80 and P240, classified as per the Federation of European Producers of Abrasives (FEPA), were used as uniform rough surfaces for modelling biofouled surfaces. The listed roughness grades were selected as they

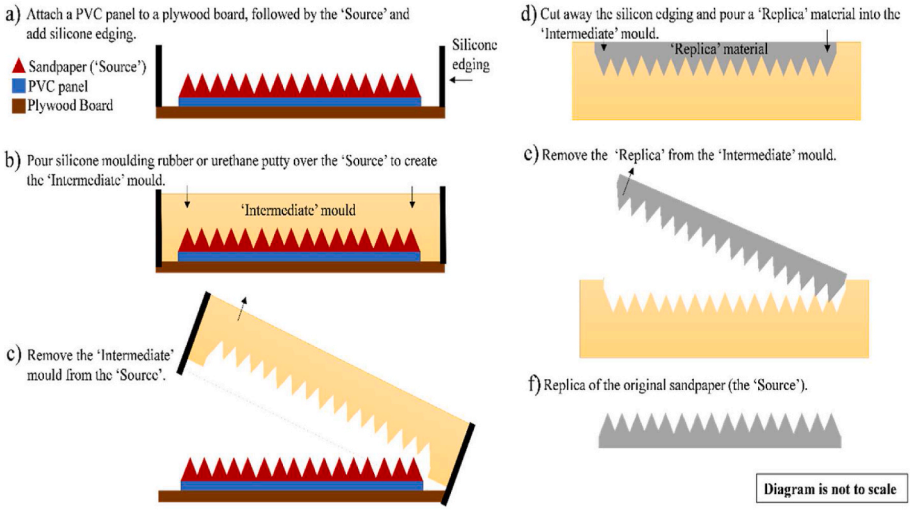

Fig. 1. Method for generating rough and smooth replicas of the sources. For illustrative purposes the example uses of sandpaper as a source, silicone moulding rubber as the intermediate material and epoxy filler as the replica material. The key in step a) shows the colours used for the Sandpaper, PVC and Plywood board across all necessary steps. (For interpretation of the references to colour in this figure legend, the reader is referred to the Web version of this article.)

have been previously used for drag experiments in the flow cell (Fabbri et al., 2019) and to cover a roughness range comparable to biofilm surface roughness values (Li et al., 2019). PVC panels were used as a smooth control for modelling an 'unfouled' surface.

To create the smooth *source* surface, a PVC panel (85 cm × 5.5 cm) was bonded to a plywood board, which formed a stable base when casting. For the rough sandpaper *sources* an individual sandpaper sheet (85 cm × 5.5 cm) was bonded to the PVC panel (Fig. 1a). For the sandpaper *source*, the PVC panel was necessary so that the resultant sandpaper *replicas* were flush with the channel walls when inserted into the flow cell.

2.1.2. Intermediate materials

Intermediate materials were poured over *source* materials to create negative moulds. There were two *intermediate* materials used. Silicone rubber (10:1 wt mix ratio of part a:b, ACC silicones, Somerset, UK) (Fig. 2) was used to cast the epoxy filler *replicas* (see *Replica* materials) and urethane putty (2.52:1 wt mix ratio of part a:b, ITW Devcon, Massachusetts, US) was used for the elastomer *replicas* (Table S1). The different *intermediate* materials were required as the elastomer *replica* material adhered to the silicone rubber *intermediate* material. In total seven *intermediate* moulds were generated: silicone-P40, silicone-P80, silicone-P240, silicone-smooth, urethane-P40, urethane-P80 and urethane-P240 (Table S1).

For the smooth elastomer *replicas*, the self-levelling material was simply brushed onto a prepped PVC panel as opposed to using a urethane-smooth *intermediate* mould.

Since the uncured silicone *intermediate* material was a liquid with a 48-h setting time, a silicone edging was built up 5 cm away from the sandpaper panel in all directions (resultant size of the *Intermediate* material mould = 95 cm × 15.5 cm) (Figs. 1 and 2). The white silicone edging was removed from the silicone *intermediate* mould once it had set to ensure flat surface for the epoxy filler *replica* material to set.

2.1.3. Replica materials

Two *replica* materials were investigated: a polydimethylsiloxane (PDMS)-based elastomer and an epoxy filler with 25% extra curing agent added. The extra curing agent was required as epoxy filler alone was too brittle for moulding and casting. Also, the epoxy filler is a commercial coating and was prepared according to manufacturer instructions for Interfill 830 (AkzoNobel, Felling, UK). A palette knife was used to fill the *intermediate* silicone mould with the epoxy filler and the elastomer was prepared and poured into the *intermediate* urethane mould.

Fig. 2. Intermediate silicone negative moulds of sandpaper-P80 and sandpaper-P240 (sources).

Upon setting in the moulds, the final *replicas* were removed with care to avoid tearing (Fig. 1e and f). As mentioned previously, a urethane-smooth *intermediate* mould was not required to generate the smooth elastomeric *replicas*.

In total, eight *replica* types were produced: elastomer-P40, elastomer-P80, elastomer-P240, elastomer-smooth, filler-P40, filler-P80, filler-P240 and filler-smooth (n = 2 to 4) that were tested in the flow cell.

The *sources*: sandpaper-P40, sandpaper-P80, sandpaper-P240 and smooth PVC (n = 2 to 4) were also tested in the flow cell to allow comparison with their material *replicas*.

2.1.4. Surface roughness measurements of sources and replicas

To confirm successful and accurate transfer of surface roughness between the *sources* and the *replicas* a blue-light interferometer (MikroCAD premium, LMI technologies, Burnaby, Canada) was used to measure arithmetical mean surface roughness height (S_a). Six area scans were taken at random sections across every 85 cm × 5 cm replicate for the *replicas* and *sources* (n = 2 to 4). A single area scan measured 10 cm × 2 cm, had an *x-z* resolution of 50 μm × 5 μm and was quantitatively analysed using ODSCAD software (GFMesstechnik GmbH, Berlin, Germany) (Fig. S1). A cut-off wavelength of 10 mm was implemented (Howell and Behrends, 2007; Medhurst, 1990). For the *sources* and *replicas*, S_a was measured both before and after exposure to a flow cell cycle. This allowed detection of any changes in roughness consequent to flow.

2.2. Preparation and mechanical characterisation of materials

Mechanical profiles were generated for both *replica* materials.

2.2.1. Tensile properties

An Instron 5969 material test instrument with a 1 kN load cell and an 87.5 mm gauge length was used for testing the mechanical properties of each material (Zou et al., 2007). The loading speed applied during testing was dependent on the material and ranged from 25 mm min^{-1} to 50 mm min^{-1}. Samples were prepared by pouring the *replica* materials into a dumbbell-shaped silicone mould. Among other calculated properties, tensile strength (MPa), failure strain (%) and elastic modulus (MPa) were of interest.

2.2.2. Wetting properties

A Data Physics optical contact angle (OCA) system was paired with SCA20 contact angle measurement software (Data Physics, GmbH, Berlin, Germany). A test material was applied to a clean 15 cm × 10 cm glass plate using a 400 μm draw-down and was exposed to drying at ambient room temperature. The OCA for each material was calculated using sessile drop testing: a 4 μL deionised water droplet was dropped onto the coated glass plate, through air, from a syringe (n = 6). For each droplet, two angle measurements were taken per second for a total of 120 s. As a reference point, the measurements taken at 60 s for each drop were used to give an average OCA for each test material.

2.2.3. Microhardness

A Fisherscope H100C hardness measurement system (Helmut Fischer, GmbH, Berlin, Germany) was used in conjunction with a WIN-HCU software. Test samples were prepared by coating PVC microslides with a test material using a 400 μm draw-down. Indentation tests were executed, and results of interest included modulus of indentation (*E*IT) (kPa), Marten's hardness (*H*M) and elastic deformation percentage of indentation energy (*n*IT).

2.3. Marine biofouling flow cell

An enclosed meso-scale flow cell (Fig. 3), with a rectangular test section of 0.85 m (L) × 0.01 m (H) × 0.05 m (W) and a recirculating tank of artificial seawater (ASW) was used for testing drag associated with sandpaper *replicas*. The ASW had a pH of 8.1 and salinity of 35‰. Although the flow cell implemented is smaller than others used in the literature (Hartenberger et al., 2020; Schultz et al., 2015), it offers high throughput experiments and enables a greater focus on understanding physico-mechanical properties of a material by allowing methods such as OCT to be used in conjunction with the flow cell, which operates at a centimetre-scale working distance. The base of the flow cell was a rigid PVC panel with acrylic side panels. A clear acrylic window panel was installed as the top plate to allow real-time OCT imaging of the *source* and *replica* surfaces in response to flow (Fabbri et al., 2018) (Fig. 3). Pressure drop sensor ports were positioned in the clear top plate 0.03 m and 0.83 m from the inlet, giving a pressure drop test length of 0.8 m. An entry length of at least 30 × flow cell height has been referenced to guarantee fully developed flow at the first pressure sensor (Hong et al., 2011), which due to the design of the flow cell could not be adopted here. The pressure sensors were located at the maximum pressure drop length to facilitate the location of the OCT and to increase pressure drop

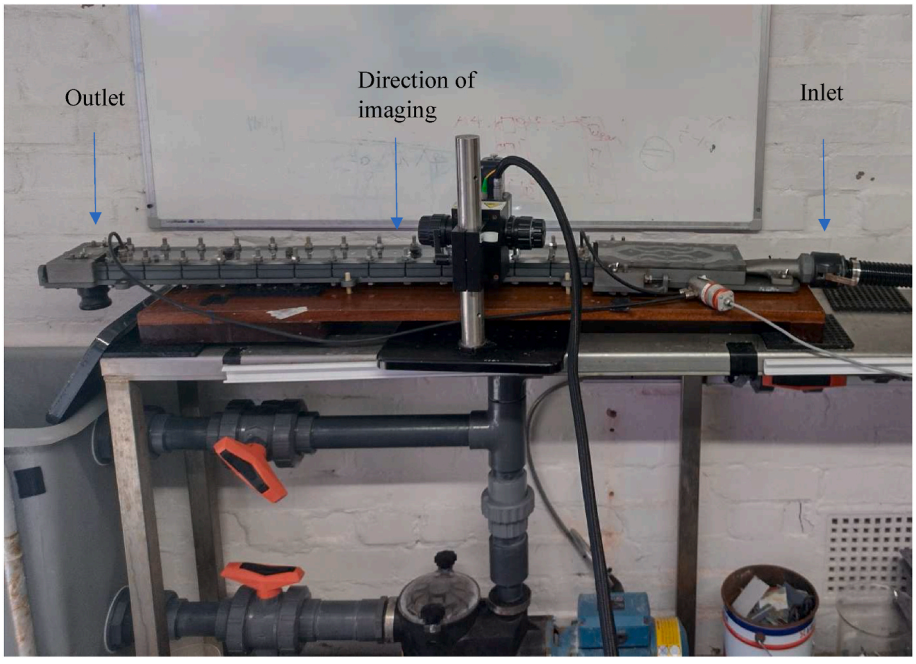

Fig. 3. Annotated diagram of the marine biofouling flow cell system (AkzoNobel, Felling, UK) used in conjunction with OCT. The OCT was set up above the flow cell fitted with a transparent top-plate to allow aerial imaging of sources and replicas within the flow cell. The inlet and outlet of water is also labelled.

sensitivity. To aid flow development a baffle was added at the flow cell inlet. The hydrodynamic characteristics have previously been investigated using sandpaper of different roughness grades (Fabbri et al., 2019).

The *source* and *replica* materials were inserted into the flow cell and exposed to a flow cycle for a duration of up to 22 min. The flow cycle involved incrementally changing the flow velocity (controlled by pump setting (centrifugal pump, 1.1 kW, Calpeda, Italy)) of ASW up to approximately 3.5 m s^{-1} (loading cycle) followed by stepwise decreases in flow velocity back to 0 m s^{-1} (unloading cycle) (Fig. S2). During the flow cycle, temperature was measured at each step and ranged between 18 °C to 24 °C. Flow velocity was recorded using a flow meter (Perfect Reef Systems Corrente+ 2" Digital flow sensor, between 0 and 150 L h^{-1}) which allows Reynolds number, *Re*, to be calculated using (Fabbri et al., 2018; Li et al., 2019; Stoodley et al., 2001):

$$Re = \frac{uD_h}{\nu_k} \tag{1}$$

where, ν_k is the kinematic viscosity of ASW (m^2 s^{-1}) at each measured temperature throughout the flow cell cycle (Fig. S2), u is average flow velocity (m s^{-1}) and D_h is the hydraulic diameter of the flow cell, calculated using the cross-sectional area and wetted perimeter of the flow cell test section. Importantly, the thickness of *sources* and *replicas* were measured using a ruler before being inserted into the flow cell; the thickness was then used to calculate the flow cell height which is used to calculate D_h. The maximum flow velocity of approximately 3.5 m s^{-1} corresponds to a maximum Re in these experiments of about 5.2×10^4 *Re*.

2.3.1. Calculating drag from pressure drop measurements

Pressure drop (ΔP) was measured throughout the flow cycle using differential pressure sensors (PL-692 Omni Instruments, between 0 and 400 mbar) that were attached to the top-plate. By measuring ΔP, the Fanning Friction Factor (C_f) could be calculated (Fabbri et al., 2019). C_f is a dimensionless number and was calculated for all flow cell runs to allow for statistical comparison.

$$C_f = \frac{D_h}{2\rho u^2}\frac{\Delta P_f}{L} \tag{2}$$

where, L is the distance between pressure ports (0.8 m) and ρ is the water density (kg m^{-3}) at the relevant temperature. In a turbulent flow regime, ΔP and u^2 can exhibit a linear dependence. Therefore, as well as calculating C_f for every stage in the flow cycle (Fig. S2), a single average C_f was calculated across an entire flow regime by substituting the slope of the line exhibited by ΔP and u^2 into Equation (2) as $\Delta P_f / u^2$ (Fabbri et al., 2019).

It is important to note that since the calculated C_f is based on an asymmetric flow cell set up (roughness is not equivalent on all walls) and there is an insufficient entry length for fully developed flow, the values reported are specific to the system used in this study. Hence, from this point C_f will be referred to as C_f* to signify that care should be taken when interpreting the C_f data. To assess the relative influence of asymmetry on C_f, flow cell experiments were also executed using a rigid rough symmetric flow cell set up, where roughness was equivalent on the top and bottom of the flow cell (please refer Supplementary Information).

2.4. Surface visualisation using Optical Coherence Tomography (OCT)

An OCT (Ganymede, ThorLabs, Germany) was set up in conjunction with the flow cell (Fig. 3) for non-invasive real-time imaging of the *sources* and *replicas* under flow conditions. An OCT scanner measures a point reflection signal from the test piece surface and produces a depth-resolved intensity profile along the scan axis (*z*-direction, flow-cell height). By acquiring several scans along-stream (*x*-direction, flow-cell length), a cross-sectional image is produced in the *xz*-plane (two-dimensional scan, 2D). Consecutive cross-sections along the other lateral axis (*y*, the flow-cell width) generates a full volumetric representation (three-dimensional scan, 3D), as detailed previously (Haisch and Niessner, 2007; Wagner et al., 2010; Xi et al., 2006). Importantly, the OCT used a LK3- LSM03(BB) objective lens which provided a central wavelength of 930 nm and gave an axial resolution of 5.8 μm and a lateral resolution of 8.0 μm, both in air (refractive index = 1). Three 2D-scans (duration 1.2 s each, OCT scan-rate = 30 kHz) were taken at every incremental and decremental steps in the flow cycle for each replicate. ThorLabs software, version 5.8.3, (Ganymede, ThorLabs, Germany) was used to control the OCT and with respect to light, focus and imaging the same settings were applied to all replicates. Milferstedt et al. (2009) determined that 3.4 mm^2 was the minimum area required for representative analysis of biofilm mesoscopic features, but also stated that an increase in area image led to higher precision (Wagner et al., 2010). Based on these recommendations, *x-z* cross-sections of 18 mm^2 (9211 × 1024 pixels) were acquired which corresponds to a resolution of 0.98 μm in the *x*-direction and 2.75 μm in the *z*-direction. As images were taken *in-situ* the refractive index for water, 1.34, was used. All OCT images were manually exported as.tiff files from ThorLabs for analysis in Fiji, ImageJ (https://imagej.net/Fiji).

2.4.1. OCT image processing and analysis

OCT datasets were processed using the open-source image analysis software, Fiji (Schindelin et al., 2012). Before processing, the 2D-scans were cropped to the area of interest containing the topographical surface features (Fig. 4). The 'Shanbhag' method was then used to threshold and binarise the images (Shanbhag, 1994) and an implemented plugin 'Find connected regions' for the factor 'Tubeness' was used to identify connected structures. The plugin 'MorphoLibJ' was used for morphology segmentation and measurements (Legland et al., 2016). Particle geometries in the 2D-images were characterised using perimeter and elongation (where a value of 1 indicates roundness, and anything higher indicates elongated structures). The same processing method was applied to all images.

2.5. Statistical analysis

R Studio (R Core Team, 2019) was used for statistical analysis. For all statistical outcomes a *P*-value of <0.05 was deemed statistically significant.

To determine differences in the mechanical profiles of the filler and elastomeric material ANOVA and post-hoc Tukey tests (95% confidence interval) were executed on the individual data sets (contact angles, tensile testing etc.). To confirm successful transfer of roughness from *sources* to *replicas,* and to determine any changes in the surface topography of *sources* and *replicas* under increasing flow, ANOVA and Post-hoc Tukey tests (95% confidence interval) were performed. For the data that did not meet the assumptions for these tests, such as non-normal distribution (Shapiro-Wilk) and unequal variance (Levene's), the non-parametric Kruskal Wallis test was used. To determine the contribution of roughness (smooth, P240, P80 and P40) and material (rigid, elastomeric) on C_f* at different *Re*, two-way ANOVA and Post-hoc Tukey tests were executed. The sum of squares of one variable was divided by the total sum of squares of all variables (elasticity, roughness, and the interaction effect) and this was multiplied by 100 to give percentage contribution.

2.6. Uncertainty analysis

Uncertainty analysis was performed on C_f* values calculated for the elastomer and filler *replicas*, sandpaper sources and smooth PVC. The uncertainty around C_f* was calculated by combining the associated uncertainty of the individual measured variables and taking the root of the sum of the squares (Cimbala, 2013). It was expected that uncertainty

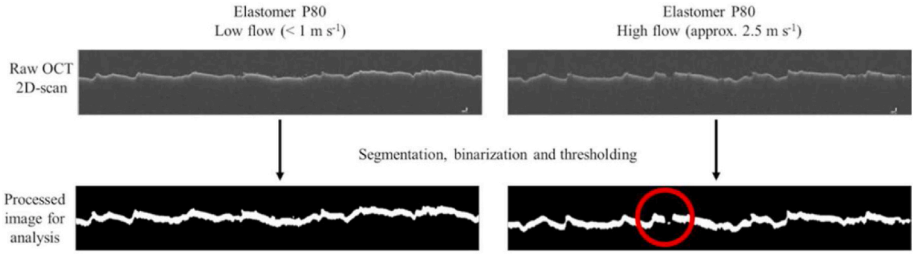

Fig. 4. Raw and processed OCT 2D-scans taken at different stages in the flow cycle. The scans for the elastomer $_{P80}$ replicas are shown as an example. The processed images are post-application of the segmentation, binarization and thresholding methods which allows for analysis of shape. The red circle shows an example of gaps in the processed images which could skew shape data. (For interpretation of the references to colour in this figure legend, the reader is referred to the Web version of this article.)

would decrease with increasing Re (Hartenberger, 2019; Lorenzini et al., 2009; Schultz et al., 2015) and therefore analysis was performed at 2.2 $\times 10^4$ and 4.0 $\times 10^4$ *Re*. The systemic and random uncertainties related to instrumental error were also calculated and are summarised in Table S2.

3. Results

3.1. Mechanical properties of synthetic materials

Two *replica* materials, a PDMS-based elastomer and epoxy filler, were mechanically characterised using an array of methods. The elastomeric material possessed a low elastic modulus and high strain to failure when compared to the epoxy filler (*P*-value < 0.05) (Table 1). The filler became torn and snapped when pulled lengthwise, as opposed to stretching as the elastomer did. This reflects the hardness of the epoxy filler which had a measured mean Marten's hardness (HM) of 21.08 $\pm$ 36.03 N mm^{-2} compared to the elastomer's 1.52 $\pm$ 0.28 N mm^{-2}. Water contact angles were used to determine material wettability. The contact angle of the filler was in the range normally associated with hydrophilic behaviour (OCA $<90°$) whereas the contact angle of the elastomer was on the border of the ranges normally associated with hydrophilic and hydrophobic behaviour (OCA $\sim$ 90°) (Law, 2014) (Table 1). As expected, the mechanical properties determined for the two materials were significantly different (*P*-value < 0.01) (Table 1). As a result, the *replica* materials were classified as elastomeric or rigid, where the rigid group comprised epoxy filler *replicas* and both *sources* (smooth PVC and sandpapers) and the elastomeric group was composed of PDMS-based elastomer *replicas* (Table 1).

3.2. Successful transfer of surface roughness from source to replica

A homogenous surface roughness for the *replicas* was achieved using sandpaper of varying roughness grades (Fig. 1). As desired, all sandpaper roughness grades used as *sources*: P40, P80 and P240 and the PVC panel, possessed significantly different S_a values (Table 1 and Fig. 5).

Blue light interferometry was used to measure S_a at all stages during the casting and moulding process, see Fig. 5. There was some evidence of a reduction in S_a during casting and moulding for some of the rougher *replicas*, for example filler-P40 and elastomer-P40 *replicas* displayed lower S_a than their *source* and *intermediate* counterparts (Fig. S1). Nevertheless, there were no statistically significant differences in S_a of the filler-P40 and elastomer-P40 *replicas* (Table 1). S_a was also measured before and after the *sources* and *replicas* were exposed to flow in the flow cell. Statistical analysis confirmed that for all test pieces ($n = 2$ to 4) there were no significant differences in surface roughness before and after flow had been applied (*P*-value > 0.05) (Fig. 5).

3.3. Changes to surface topography of material replicas in response to applied flow

OCT 2D-scans were taken of the *sources* and *replicas* under increasing flow in the flow cell. Raw images were then processed to quantify topographical features at the mesoscale. Note that in some OCT images the boundary surface was lost (Fig. 4 and S3) which influenced data output, therefore images with missing sections were excluded from statistical analysis. Also, although roughness was consistent across all *source* and *replica* replicates ($n = 2$ to 4), shape data produced significantly different numeric results between replicates. Therefore, to study changes in shape parameters with increasing flow velocity, averages could not be meaningfully taken, and individual structures in fields of view for each replicate were analysed separately.

Table 1
Summary of source and replica materials, including roughness measurements, mechanical properties, and classification of materials as elastomeric or rigid. The intermediate material is that which was used to create a replica of the source using a mould. A dash indicates that data was not collected, or it was not applicable.

	Roughness (FEPA standards)	Measured roughness pre-flow (S_a, μm)	Elastic modulus (MPa)	Ultimate tensile strain (%)	Tensile strength (MPa)	Contact angle (°)	Marten's Hardness (N mm^{-2})	Classification	Intermediate material
Source									
Polyvinyl chloride (PVC)	Smooth	6.8 ± 0.9	~3500 [a]	–	–	–	–	Rigid	–
Sandpaper	P240	16.3 ± 1.7	~200,000–400,000	–	–	–	–	Rigid	–
Sandpaper	P80	48.9 ± 1.3							–
Sandpaper	P40	107.7 ± 3.5							
Replica									
PDMS-based elastomer	Smooth	6.3 ± 1.2	1.54 ± 0.26	135.3 ± 23.3	1.04 ± 0.15	87.8 ± 15.1	1.52 ± 0.28	Elastomer	Urethane putty
	P240	16.0 ± 1.4							
	P80	44.9 ± 1.3							
	P40	93.7 ± 5.5							
Epoxy filler + 25% extra curing agent	Smooth	4.9 ± 1.7	63.23 ± 11.06	14.14 ± 2.2	2.91 ± 0.14	78.1 ± 12.8	21.07 ± 6.03	Rigid	Silicone moulding rubber
	P240	14.8 ± 2.0							
	P80	42.7 ± 2.3							
	P40	92.4 ± 6.6							

[a] Value taken from Titow (1984) for rigid PVC.

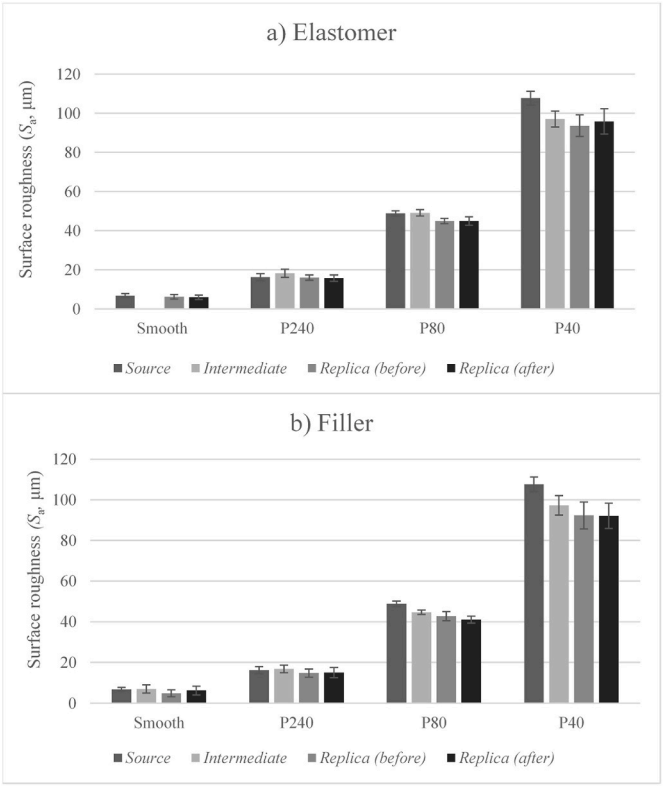

Fig. 5. Surface roughness ($S_{a,\ \mu m}$) measured using a blue-light interferometer for a) elastomer replicas and b) filler replicas before and after a flow cycle on the flow cell. The S_a of their counterpart sources and intermediates is also shown, for all roughness' investigated: smooth, P240, P80 and P40.

Image analysis revealed that despite roughness profiles being substantially similar between elastomeric and filler *replicas* of the same roughness category (Table 1), the surface shape was significantly different (P-value < 0.05), especially at higher roughness grades (P40 and P80) (Fig. 6). The elastomer *replicas* appeared wave-like whereas the filler *replicas* more closely resembled a sandpaper surface (Fig. 6). Similarities between the sandpaper *sources* and filler *replicas* were enhanced when assessing structural changes consequent to changing flow velocity as both datasets exhibited a linear relationship between elongation and flow velocity. In contrast, the elastomer *replicas* showed fluctuations in elongation values with increasing flow velocity as the surface appeared roughened and surface peaks moved (Fig. 7).

Interestingly, the elastomer-P40 *replicas* showed signs of permanent deformation, as illustrated by 2D-scans taken of the elastomer-P40 after cessation of flow (Fig. 7). A relaxation period was not included during the experiments, yet it does not seem likely from the example depicted in Fig. 7 that there would be full recovery of the initial structure. From the elongation data collected during the loading and unloading cycle there is evidence of some elastic rebound which is indicative of a viscoelastic response to applied flow. However, further experimentation would be required to confirm these observations.

3.4. Drag induced by sources and replicas in an asymmetric flow cell system

3.4.1. Elasticity

Loading cycle data were obtained for all the elastomeric and rigid test pieces (smooth, P240, P80 and P40, see Table 1 and Fig. 8). The ΔP measurements were expressed as C_f and were plotted against Re (Fig. 8).

For most test pieces the general shape of the drag curves was broadly similar; with increasing Re there was a slowing decrease in C_f* (Fig. 8). However, under closer inspection of the data points in Fig. 8, filler-P40, elastomer-P40, -P80 and -P240 data demonstrate longer Re dependence where at approximately 3.0×10^4 *Re*, C_f drops off. It is known from profilometry (Fig. 5) and OCT-scans (Fig. 6) that S_a was not affected by flow (Fig. 5) and therefore this dependence was linked to a mechanical response to increasing shear stress, which is not demonstrated by the rigid test pieces.

More specifically, a single average C_f* was calculated for all *replicas* and *sources* ran on the flow cell using the slope of the line when ΔP was plotted against u^2 using Equation (2). This was possible as the relationship between ΔP and u^2 was linear for all flow cell runs. The elastomer-P80 and -P240 led to a 52% and 48% increase in average C_f* when compared to the rigid counterparts of substantially similar roughness (Fig. 9). Despite a significant increase in roughness elastomer-P40 displayed a drop in C_f* when compared to elastomer-P80 and was only 2% higher than rigid-P40 (Fig. 9). Also, elastomer-smooth, and rigid-smooth replicas demonstrated little to no Re dependence (Figs. 3 and 4) and possessed only a 6% difference in average C_f* (P-value > 0.5) (Fig. 9).

3.4.2. Roughness

The C_f* of the elastomeric replicas was significantly higher than the C_f* of the rigid counterparts up to a roughness of approximately 45 µm (P80 data) (Fig. 8), and both data sets exhibited a positive relationship between S_a and C_f* (Fig. 9). The average C_f* calculated for the rigid-P240, -P80 and -P40 test pieces were 14%, 59% and 100% higher than the rigid-smooth *replicas* and for the elastomeric data set these values were 60%, 127% and 93%, respectively. It is important to note that although there was a strong linear relationship between average S_a

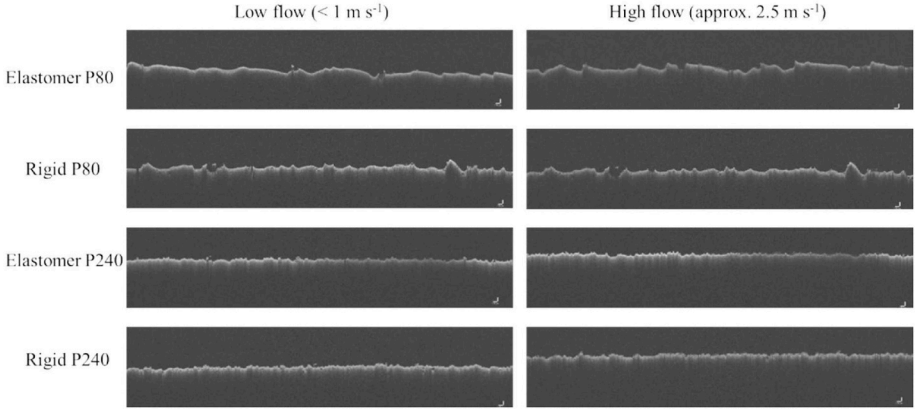

Fig. 6. Raw OCT 2D-scans taken at low and high flow during a flow cell cycle. The elastomer-P80, elastomer-P240, filler-P80 and filler-P240 have been used as examples to show changes in the surface topography.

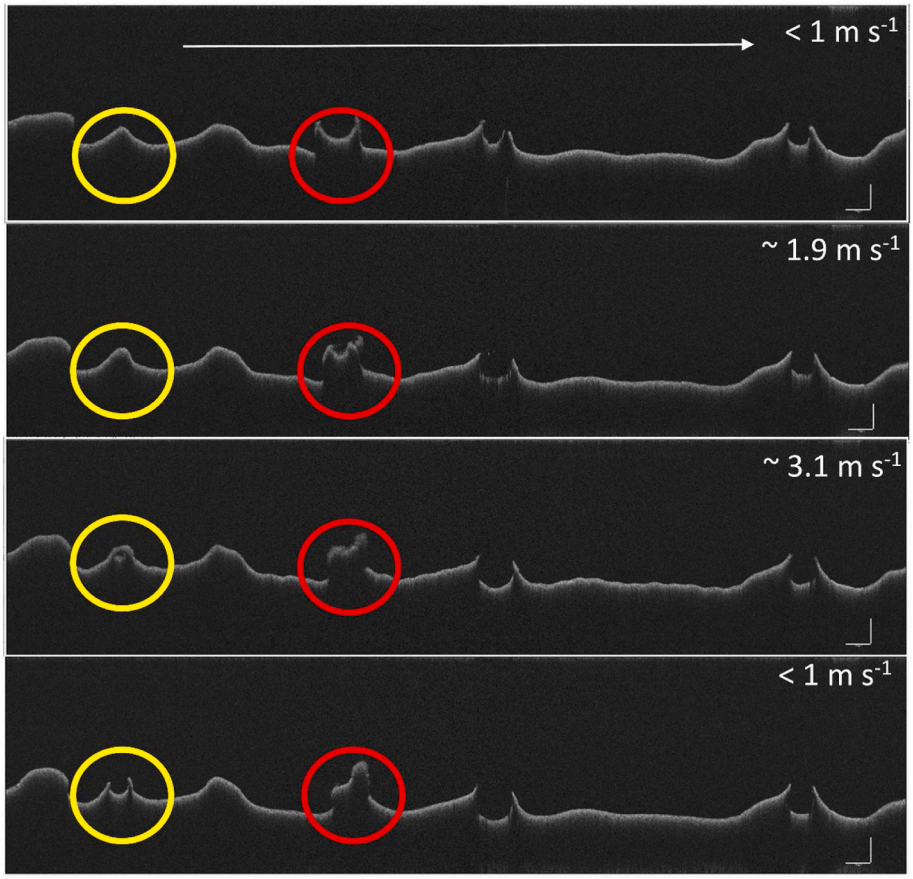

Fig. 7. OCT 2D-scans taken at different flow velocities during a flow cell cycle. An elastomer-P40 replicate (n = 2) has been used to show a change in surface topographical features at different stages. A flow velocity of < 1m s^{-1} indicates the start and end of the flow cell cycle. Maximum elongation was determined at ~1.9 m s^{-1} and the maximum flow velocity reached was 3.1 m s^{-1}. Changes of two prominent features are circled (red and yellow rings) at each flow stage. (For interpretation of the references to colour in this figure legend, the reader is referred to the Web version of this article.)

and average C_f* for the rigid data set ($R^2 = 0.99$), it was poor for the elastomeric data set, due to the P40 *replica* drag data ($R^2 = 0.49$) (Fig. 9).

The non-linearity between S_a and average C_f* of the elastomer *replicas* suggests that the elastic material properties enhanced the effects of roughness (Fig. 9), as elastomer *replicas* showed comparable C_f* values to filler *replicas* in the next roughness category: elastomer-P240 and -P80 displayed behaviour comparable to filler-P80 and -P40 (Figs. 8 and 9). It was concluded that material properties and surface roughness influenced drag, taken as a single C_f* value, both independently (*P*-value < 0.01) and combined (*P*-value < 0.01). This conclusion was supported using interaction plots produced in R studio (*P*-value < 0.001). Importantly, the parameter of shape was not introduced into the ANOVA as it showed co-linearity with the roughness values.

3.4.3. Contribution of elasticity and roughness to drag

To assess the contribution of material properties and roughness on C_f* with increasing *Re*, C_f* was calculated for specified Re and two-way ANOVAs were carried out. For all Re investigated (covering the range from about to 2.0×10^4 to 5.2×10^4 *Re*), roughness, material-type, and an interaction between the two factors was significant in effecting average C_f* (*P*-value < 0.01). Table 2 shows how the effect of both roughness and material evolves with increasing Re (measured as percentage contributions) at specified *Re*, for example the roughness contribution appears to increase and plateau, and the material contribution fluctuates. Interestingly, the combined effect of material and roughness declined with increasing *Re*.

3.4.4. Uncertainty analysis of C_f*

Uncertainty analysis was performed on the average C_f* values taken at 2.2×10^4 and 4.0×10^4 Re for all material *replicas* and *sources*. Uncertainty bounds for the elastomeric *replicas* ranged from ±22% at the lower Re and ±15% at the higher *Re*. For the filler *replicas* the uncertainty values were ±28% and 25% and the *source* data (sandpaper and smooth PVC) uncertainty was ±33% and 28%. The uncertainty bounds reported here are higher than those reported by Hartenberger (2019) which could be a consequence of the asymmetric boundaries and small aspect ratio of the channel. For further details on the uncertainty error around C_f* taken at different Re please refer to Table S3.

4. Discussion

4.1. The mechanical characterisation and visualisation of the elastomer and filler material

As intended, the PDMS-based elastomer and epoxy filler displayed significantly different mechanical properties (Table 1) and from these results it is suggested that the elastomer would be better suited to modelling biofilm behaviour than rigid structures. For example, the elastomer demonstrated a high tensile strain, within the range of between 150% and 320% recorded for natural biofilms (Ohashi et al., 1999), and possessed a lower elastic modulus than the rigid counterparts (Table 1). In addition, whilst the filler demonstrated hydrophilic behaviour (OCA <90°) (Table 1), the contact angles for the elastomer sat either side of the 90° threshold, which is comparable to the wetting behaviour observed for natural biofilms (Werb et al., 2017).

Biofilms are known to exhibit different degrees of elasticity, ranging from Pa to kPa (Table S4). To date, rheological data does not exist for ship-relevant marine biofilms. Souza-Egipsy et al. (2021) however, compared mechanical properties for eukaryotic and prokaryotic biofilms obtained from an acidic stream, and found that the elastic modulus for the eukaryotic biofilms was significantly lower than the prokaryotic biofilms. Marine biofilms incorporate eukaryotic organisms and therefore it is possible that they would possess a different elastic modulus to what has been reported in the literature for biofilms found in other

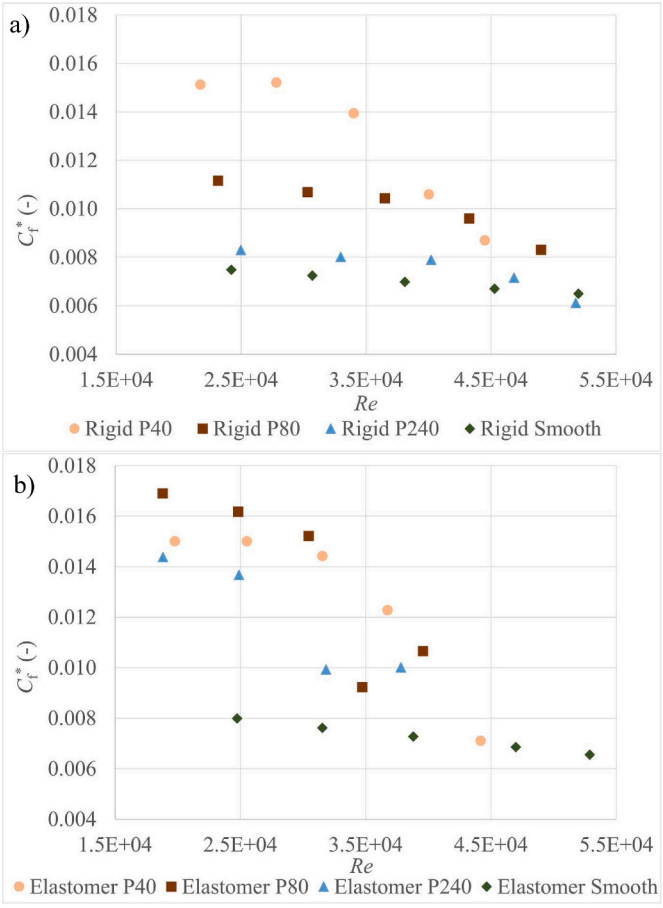

Fig. 8. C_f plotted against Re for all sources and replicas tested in the flow cell (n = 2 to 4); a) shows data for the elastomeric replicas and b) is the rigid dataset; where circles represent the P40 data, squares are P80, triangles are P240, and a dash is for the smooth data. Only loading data is plotted in both figures and a power line of best fit has been applied to each data set. Re and C_f were calculated for every step in the flow cell loading cycle (Fig. S2) using Equation (1) andEquation (2).

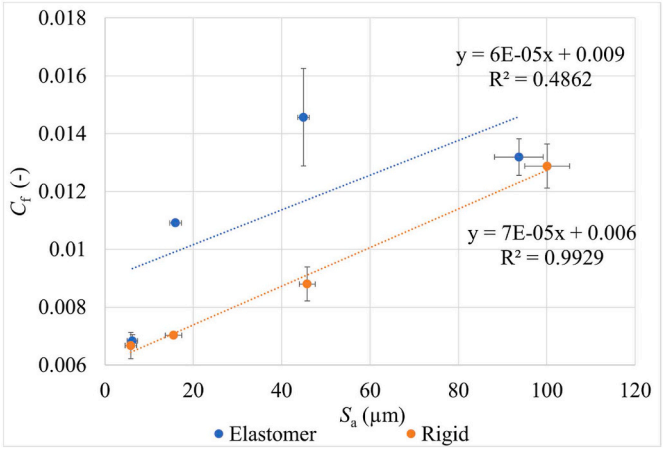

Fig. 9. Average S_a (µm) ± SD plotted against average C_f (−) ± SD (n = 2 to 4) for the elastomeric and rigid material categories, where rigid includes the filler replica data and source data. Data for four roughness' are shown: smooth, P240, P80 and P40 (as per FEPA standards). Average C_f was calculated by substituting the slope of ΔP and u^2 into Equation (2) for all replicates. A linear line of best fit has been applied.

Table 2
The contribution of material, roughness, and the interaction of the two on C_f calculated at three different Re using power lines of best fit from Fig. 8. All values are percentages (%).

	2.2×10^4 Re	3.0×10^4 Re	4.0×10^4 Re
Material	18.5	12.6	18.6
Roughness	55.9	76.7	75.6
Interaction	25.6	10.7	5.8

environments, for example medical and wastewater treatment (Table S4). It is of interest to mechanically characterise marine biofilms to inform future design of materials that could be used in the proposed synthetic *replica* system for modelling biofilm physico-mechanical responses to applied flow.

4.2. Drag induced by rough elastomeric sandpaper replicas

Typically, computational and experimental studies have utilised rigid, rough surfaces such as sandpaper or sand-grains for studying drag, namely biofilm-associated drag (Yusim and Utama, 2017). In part, this is explicable by work that has shown parallels between drag induced by rigid structures and biofilms (Flack et al., 2007; Hartenberger et al., 2020).

Flow cells are widely used to study impacts of surface roughness on skin friction and drag. A symmetric flow cell set up is often implemented, where the top and base plate are of equivalent surface roughness. However, in this study, C_f* was calculated in an asymmetric flow cell, where the smooth top plate acted as a window into the flow cell and the base plate was rough; this was necessary to allow real-time visualisation and *in-situ* measurements of surface deformation. The side walls were also smooth since it was impractical to line these with *source* or *replica* materials due to the narrow dimensions. The compromise of having an optically clear window wall to allow observation has been recognised in other studies (Blauert, 2017; Picioreanu et al., 2018) and has been corrected for using techniques such as Particle Image Velocimetry (PIV) (Hartenberger et al., 2020). The authors acknowledge that the C_f* calculated in the present study for the rough surfaces will likely be underestimations of the values obtained in a flow cell where roughness is equivalent on all walls. Nevertheless, despite this limitation we believe C_f* is a useful metric for comparing relative effect of drag by the different materials, at least over the Re range of 2.0×10^4 to 5.2×10^4 studied here.

It would be of interest to determine a relationship between C_f* for a symmetric and asymmetric flow cell system using the elastic and rigid materials (Fig. S4) with the purpose of calculating roughness-functions and predicting drag at a ship-relevant scale.

4.2.1. Surface roughness and drag

It is well known that a surface with higher roughness will induce greater drag due to increased friction; this has been observed at laboratory and ship scale (McEntee, 1916; Moody, 1944; Oliveira et al., 2018; Townsin, 2003). As expected, this trend was observed for the elastomeric and rigid datasets collected here (Figs. 8 and 9). The calculated drag for elastomer-smooth, rigid-smooth and the PVC-smooth was broadly consistent (P-value > 0.5) (Figs. 8 and 9), showing little to no impact from the different mechanical properties.

For the rigid and elastic data sets, once roughness was introduced there was a jump in the C_f* values (Figs. 8 and 9). This increase was different depending on the material. As is characteristic for a rigid structure the rigid data set displayed a strong positive linear relationship between S_a and C_f* (Fig. 9) (Fabbri et al., 2019). The elastomer *replica* C_f* data, however, demonstrated a non-linear relationship with increasing S_a which was partly explicable by the 15% drop in C_f* between elastomer-P80 and -P40 (Fig. 9). As roughness was controlled, the deviation was attributed to mechanical properties, namely elasticity and

the response of topographical features under flow (Fig. 7). This conclusion is supported by ANOVA which indicated a significant relationship between static roughness (before and after flow) and material type on C_f* at specified Re (P-value < 0.001). Hartenberger et al. (2020) similarly interpreted their experimental comparisons between living biofilms and their rigid replicas where they concluded that differences in drag were driven by compliance, namely mat vibrations, and streamer flutter.

The differences observed between the elastomeric and rigid data sets highlight how rigid structures are limited for studying drag associated with softer materials. For example, if the line of best fit for the rigid dataset had been utilised to predict drag for the elastomeric system (Fig. 9), then average C_f* would have been significantly underestimated. Further, Fabbri et al. (2019) found a linear relationship between rigid roughness and drag, yet if this had been used to extrapolate drag associated with an elastomeric surface, the resultant drag values would have also been underestimated. The results presented over our Re range of 2.0×10^4 to 5.2×10^4 Re demonstrate how not only roughness but physico-mechanical properties must be considered when predicting drag (Jafari et al., 2018; Picioreanu et al., 2018); and that physico-mechanical properties could have a larger impact on C_f than initially expected.

4.2.2. Elasticity and drag

Viscoelastic structures such as biofilms will induce a greater pressure drop, and therefore drag, than rigid structures such as sandpaper or sand grains, as a consequence of their physico-mechanical properties (Hansen and Hunston, 1974; Peterson et al., 2015). An early study by Picologlou et al. (1980) experimented with biofilms and turbulent pipes and concluded that when the viscoelasticity of biofilms was considered, as opposed to assuming rigidity (in the form of sand grains), the resultant frictional resistance was higher. More recently, Hartenberger et al. (2020) reached a similar conclusion when comparing natural biofilms to 3D-printed rigid replicas; biofilms displayed a significantly higher drag than their rigid replicas and displayed a different trend in drag with increasing *Re.* This implies the behaviour of a biofilm under increasing flow velocity cannot be fully captured by rigid replicas even if equivalent surface topography is achieved. Similarly, Yeginbayeva et al. (2020) studied the combined effect of mimicked 'hull' roughness and biofilms and found biofilm presence to be significant in affecting drag. The data presented in the current study supports these conclusions as differences in drag curves were observed between the elastomeric and rigid *replicas* (Fig. 8).

Perkins et al. (2012) studied biofouled hydropower pipes and determined that with increasing *Re,* C_f either increased or plateaued until a critical Re was reached. After this critical point, C_f experienced a sudden drop with increasing Re that eventually levelled out again (Lambert et al., 2009; Perkins et al., 2012). The authors reasoning for this behaviour was that the biofilm had been sheared, had detached from the surface or was being flattened against the pipe wall. Interestingly, a similar drag curve to those presented for biofouled pipes by Perkins et al. (2012) was observed for the homogenous, rough elastomer *replicas*, where up to a Re of 3.0×10^4 the elastomeric drag curves were plateaued and past this Re the value of C_f* experienced a sudden decline. This decline is assumed to be due to a physico-mechanical response, such as streamlining or flattening out, as unlike real biofilms, detachment was not possible, and roughness remained unchanged before and after the surfaces were subject to flow (Fig. 5). This is supported by results of a two-way ANOVA that showed distinct changes to the contributions of roughness and material-type to C_f* at a Re of 3.0×10^4. Also, the elastomeric drag curves did not level out at higher Re (Fig. 8), therefore future flow cell runs could be set up to operate at greater Re which would perhaps identify a Re at which the elastomer *replicas* responses plateau and show no Re dependence.

It is worth noting that in Perkins et al. (2012) shearing and flattening behaviour was not physically observed during flow and therefore it is important to consider that the trend between C_f* and Re observed for the elastomeric data, which was attributed to compliance, could explain what has been observed in the heterogeneous biofilm study.

The conclusion that differences in C_f* induced by the elastomeric and filler *replicas* was consequence to different mechanical profiles and therefore physico-mechanical responses to flow is supported by analysis of the OCT-images. The filler and elastomeric *replicas* experienced different responses to increasing flow velocity as shown by changes to their surface topography (Fig. 6). When tested on the flow cell, the elastomeric *replicas* did not deform to the same degree as natural biofilms, which are generally softer and more elastic (Table S4), and removal was not observed, yet there was evidence of a viscoelastic response to increasing flow velocity (Fig. 7). It would be beneficial to use an OCT to measure deformation quantitively using angles of deformation, as did Blauert (2017), or alternative image analysis methods, such as Digital Image Correlation (DIC). DIC could provide information on 2D and 3D-interactions between a compliant surface and surrounding fluid which would inevitably alter C_f. Nevertheless, the results presented in the current study demonstrate how fluid structure interactions vary depending on material mechanical properties (Fig. 6) and can evolve with increasing flow velocity (Fig. 7 and Table 2).

This study is the initial basis for addressing questions such as: what happens to a biofilm surface under flow, and how do the physical and mechanical properties respond? The authors detail a successful quick and easy moulding and casting process for generating material replicas and would be suited to experimental up-scaling. We acknowledge that the synthetic model is in its primary stages, but by controlling roughness and mechanical properties of different materials we believe it is easier to separate out the relative contribution of these properties on drag than if we had used a heterogeneous surface, or one that allowed sloughing and detachment. We aim to add further structural and mechanical complexity to better mimic real biofilms in future work. Also, future studies should look to compare the data obtained from the meso-scale flow cell to that collected for a larger flow cell (with a suitable entry length to guarantee fully developed flow), to validate its use.

5. Conclusion

Surface roughness and physico-mechanical properties influence drag. What is unknown is how they interact with each other, and how this relationship influences drag. A method for generating a fully synthetic model system for studying the effects of physico-mechanical properties on drag has been presented. Sandpaper of varying roughness grades was chosen as the template for moulding, as it is a readily available rigid roughened surface with homogenous coverage and controlled roughness characteristics.

Although biofilms have not been investigated here, the *replica* data produced supports the hypothesis that elastomeric surfaces are better substitutes than rigid structures for modelling elastic or viscoelastic responses to drag. This was captured by a pressure drop system and OCT 2D-scans, where the movement of topographical features was detected under flow. The combination of studying mesoscopic structural parameters (such as elongation) extracted from OCT 2D-scans, and the mechanics of elastomeric materials allows us to represent natural biofilm physico-mechanics more closely, within a dynamic environment (a flow cell).

The rigid data showed significantly lower C_f* values than the elastomeric counterparts (Fig. 9) and would have been ineffective in predicting C_f* associated with the elastomeric *replicas*. As the elastic modulus of the materials was significantly different (P-value < 0.001) (Table 1), while roughness (S_a) was the same (Fig. 5 and Table 1), it was concluded that the elasticity played a significant role in influencing the drag (Figs. 8 and 9), as it may be expected to do in natural biofilms (Hartenberger, 2019; Rupp et al., 2005). This was confirmed by statistical analysis that deemed roughness and elasticity (independently and combined) were both significant in affecting C_f*.

Our results showed that elasticity is significant in influencing drag and shares a significant interaction with surface roughness and thus material properties should not be neglected in predicting drag caused by viscoelastic biofilms or in model systems. This knowledge serves as a basis for future study into the effect of physico-mechanical properties of compliant materials on drag, it should be used to inform future models and is relevant to the coating industry with respect to targeting specified biofilm properties for reducing biofilm presence on ship hulls.

CRediT authorship contribution statement

Alexandra Snowdon: Conceptualization, Methodology, Validation, Formal analysis, Investigation, Resources, Writing – original draft, Writing – review & editing, Visualization. **Shi-Qi An:** Formal analysis, Investigation. **Alistair Finnie:** Writing – review & editing. **Marie Dale:** Methodology, Writing – review & editing. **Simon Dennington:** Methodology, Writing – original draft, Writing – review & editing. **Jennifer Longyear:** Conceptualization, Methodology, Resources, Writing – original draft, Writing – review & editing, Supervision, Funding acquisition. **Julian Wharton:** Conceptualization, Methodology, Writing – original draft, Writing – review & editing, Supervision, Funding acquisition. **Paul Stoodley:** Conceptualization, Methodology, Writing – original draft, Writing – review & editing, Funding acquisition.

Declaration of competing interest

The authors declare the following financial interests/personal relationships which may be considered as potential competing interests: The work was sponsored, in part, by AkzoNobel through Paul Stoodley. Employees of AkzoNobel were involved in the work (Jennifer Longyear, Marie Dale and Alistair Finnie).

Data availability

A DOI has been provided in the Supplementary information. All data supporting this study will be available from the University of Southampton repository at https://doi.org/10.5258/SOTON/D2287

Acknowledgements

This work was funded by a DTP ESPRC grant EP/R513325/1 to the University of Southampton with partial funding from NBIC/BBSRC 01POC18032 and AkzoNobel. The authors would like to thank Dr Kevin Reynolds of AkzoNobel for the design of the elastomers used and Dr Hao-Liang Chen for editorial review.

Appendix A. Supplementary data

Supplementary data to this article can be found online at https://doi.org/10.1016/j.oceaneng.2022.112739.

References

Andrewartha, J., Perkins, K., Sargison, J., Osborn, J., Walker, G., Henderson, A., Hallegraeff, G., 2010. Drag force and surface roughness measurements on freshwater biofouled surfaces. Biofouling 26, 487–496. https://doi.org/10.1080/08927014.2010.482208.

Berlanga, M., Guerrero, R., 2016. Living together in biofilms: the microbial cell factory and its biotechnological implications. Microb. Cell Factories. https://doi.org/10.1186/s12934-016-0569-5.

Blauert, F., 2017. Investigating Biofilm Deformation Using Optical Coherence Tomography and Fluid-Structure Interaction Simulation.

Blauert, F., Horn, H., Wagner, M., 2015. Time-resolved biofilm deformation measurements using optical coherence tomography. Biotechnol. Bioeng. 112, 1893–1905. https://doi.org/10.1002/bit.25590.

Cimbala, J.M., 2013. Experimental uncertainty analysis [WWW Document]. Math. Mech. Eng.

Depetris, A., Wiedmer, A., Wagner, M., Schäfer, S., Battin, T.J., Peter, H., 2019. Automated 3d optical coherence tomography to elucidate biofilm morphogenesis over large spatial scales. JoVE. https://doi.org/10.3791/59356, 2019.

Di Martino, P., 2018. Extracellular polymeric substances, a key element in understanding biofilm phenotype. AIMS Microbiol 4, 274–288. https://doi.org/10.3934/microbiol.2018.2.274.

El-Labbad, A.F., 1987. Techno Economic Analysis of the Problems of the Bottom Maintenance of Ships. Newcastle University.

Fabbri, S., Dennington, S., Price, C., Longyear, J., Stoodley, P., 2019. A marine biofilm flow cell for in situ determination of drag and biofilm structure. Ocean Eng. 178, 59–65. https://doi.org/10.1016/j.oceaneng.2019.02.066.

Fabbri, S., Dennington, S.P., Price, C., Stoodley, P., Longyear, J., 2018. A marine biofilm flow cell for in situ screening marine fouling control coatings using optical coherence tomography. Ocean Eng. 170, 321–328. https://doi.org/10.1016/j.oceaneng.2018.10.030.

Flack, K.A., Schultz, M.P., Connelly, J.S., 2007. Examination of a critical roughness height for outer layer similarity. Phys. Fluids 19. https://doi.org/10.1063/1.2757708.

Flemming, H.C., Wingender, J., 2010. The biofilm matrix. Nat. Rev. Microbiol. https://doi.org/10.1038/nrmicro2415.

Gloag, E.S., German, G.K., Stoodley, P., Wozniak, D.J., 2018. Viscoelastic properties of Pseudomonas aeruginosa variant biofilms. Sci. Rep. 8, 1–11. https://doi.org/10.1038/s41598-018-28009-5.

Haisch, C., Niessner, R., 2007. Visualisation of transient processes in biofilms by optical coherence tomography. Water Res. 41, 2467–2472. https://doi.org/10.1016/j.watres.2007.03.017.

Hansen, R.J., Hunston, D.L., 1974. An experimental study of turbulent flows over compliant surfaces. J. Sound Vib. 34, 297. https://doi.org/10.1016/S0022-460X(74)80314-7. -IN2.

Hartenberger, J., 2019. Drag Production of Filamentous Biofilm by. University of Michigan.

Hartenberger, J.D., Callison, E.G., Gose, J.W., Perlin, M., Ceccio, S.L., 2020. Drag production mechanisms of filamentous biofilms. Biofouling. https://doi.org/10.1080/08927014.2020.1806250.

Haslbeck, E.G., Bohlander, G.S., 1992. Microbial Biofilm Effects on Drag, Ship Production Symposium.

Hong, J., Katz, J., Schultz, M.P., 2011. Near-wall turbulence statistics and flow structures over three-dimensional roughness in a turbulent channel flow. J. Fluid Mech. 667, 1–37. https://doi.org/10.1017/S0022112010003988.

Howell, D., Behrends, B., 2007. A review of surface roughness in antifouling coatings illustrating the importance of cutoff length. Biofouling 22, 401–410. https://doi.org/10.1080/08927010601035738.

Jafari, M., Desmond, P., van Loosdrecht, M.C.M., Derlon, N., Morgenroth, E., Picioreanu, C., 2018. Effect of biofilm structural deformation on hydraulic resistance during ultrafiltration: a numerical and experimental study. Water Res. https://doi.org/10.1016/j.watres.2018.08.036.

Kandemir, N., Vollmer, W., Jakubovics, N.S., Chen, J., 2018. Mechanical interactions between bacteria and hydrogels. Sci. Rep. 8 https://doi.org/10.1038/s41598-018-29269-x.

Körstgens, V., Flemming, H.C., Wingender, J., Borchard, W., 2001. Uniaxial compression measurement device for investigation of the mechanical stability of biofilms. J. Microbiol. Methods 46, 9–17. https://doi.org/10.1016/S0167-7012(01)00248-2.

Lambert, M.F., Edwards, R.W.J., Howie, S.J., De Gilio, B.B., Quinn, S.P., 2009. The impact of biofilm devlopment on pipe roughness and velocity profile. In: Proc. World Environ. Water Resour. Congr. 2009 - World Environ. Water Resour. Congr. 2009 Gt. Rivers, vol. 342, pp. 122–134. https://doi.org/10.1061/41036(342)13.

Law, K.-Y., 2014. Definitions for hydrophilicity, hydrophobicity, and superhydrophobicity: getting the basics right. J. Phys. Chem. Lett. 5, 686–688. https://doi.org/10.1021/jz402762h.

Legland, D., Arganda-Carreras, I., Andrey, P., 2016. MorphoLibJ: integrated library and plugins for mathematical morphology with ImageJ. Bioinformatics 32, 3532–3534. https://doi.org/10.1093/BIOINFORMATICS/BTW413.

Lewkowicz, A.K., Das, D.K., 1986. Turbulent boundary layers on rough surfaces with and without a pliable overlayer: a simulation of marine fouling. Int. Shipbuild. Prog. 33, 174–186. https://doi.org/10.3233/ISP-1986-3338601.

Li, C., Atlar, M., Haroutunian, M., Norman, R., Anderson, C., 2019. An investigation into the effects of marine biofilm on the roughness and drag characteristics of surfaces coated with different sized cuprous oxide (Cu_2O) particles. Biofouling 35, 15–33. https://doi.org/10.1080/08927014.2018.1559305.

Lorenzini, M., Morini, G.L., Henning, T., Brandner, J., 2009. Uncertainty assessment in friction factor measurements as a tool to design experimental set-ups. Int. J. Therm. Sci. 48, 282–289. https://doi.org/10.1016/J.IJTHERMALSCI.2008.06.006.

Macedo, R.G., Robinson, J.P., Verhaagen, B., Walmsley, A.D., Versluis, M., Cooper, P.R., van der Sluis, L.W.M., 2014. A novel methodology providing insights into removal of biofilm-mimicking hydrogel from lateral morphological features of the root canal during irrigation procedures. Int. Endod. J. 47, 1040–1051. https://doi.org/10.1111/IEJ.12246.

McEntee, W., 1916. Variation of frictional resistance of ships with condition of wetted surface. J. Am. Soc. Nav. Eng. https://doi.org/10.1111/j.1559-3584.1916.tb00632.x.

Medhurst, J.S., 1990. Outline of a draft international standard for the measurement and characterisation of roughness topography in fluid flow. In: International Workshop on Marine Roughness and Drag, pp. 1–9.

Milferstedt, K., Pons, M.N., Morgenroth, E., 2009. Analyzing characteristic length scales in biofilm structures. Biotechnol. Bioeng. 102, 368–379. https://doi.org/10.1002/bit.22075.

Moody, L.F., 1944. Friction factors for pipe flow. Trans. ASME 66, 671–684.

Murphy, E.A.K., Barros, J.M., Schultz, M.P., Flack, K.A., Steppe, C.N., Reidenbach, M.A., 2018. Roughness effects of diatomaceous slime fouling on turbulent boundary layer

hydrodynamics. Biofouling 34, 976–988. https://doi.org/10.1080/08927014.2018.1517867.
Ohashi, A., Koyama, T., Syutsubo, K., Harada, H., 1999. A novel method for evaluation of biofilm tensile strength resisting erosion. In: Water Science and Technology. Elsevier Science Ltd, pp. 261–268. https://doi.org/10.1016/S0273-1223(99)00176-6.
Oliveira, D., Larsson, A.I., Granhag, L., 2018. Biofouling the Journal of Bioadhesion and Biofilm Research Effect of ship hull form on the resistance penalty from biofouling Effect of ship hull form on the resistance penalty from biofouling. Biofouling 34, 262–272. https://doi.org/10.1080/08927014.2018.1434157.
Perkins, S.C.T., Henderson, A.D., Walker, J.M., Li, X.L., 2012. The influence of bacteria based biofouling on the wall friction and velocity distribution of hydropower pipes. Australas. J. Mech. Eng. 12, 77–88. https://doi.org/10.7158/M12-087.2014.12.1.
Peterson, B.W., He, Y., Ren, Y., Zerdoum, A., Libera, M.R., Sharma, P.K., van Winkelhoff, A.J., Neut, D., Stoodley, P., van der Mei, H.C., Busscher, H.J., 2015. Viscoelasticity of biofilms and their recalcitrance to mechanical and chemical challenges. FEMS Microbiol. Rev. https://doi.org/10.1093/femsre/fuu008.
Peterson, B.W., van der Mei, H.C., Sjollema, J., Busscher, H.J., Sharma, P.K., 2013. A distinguishable role of eDNA in the viscoelastic relaxation of biofilms. mBio 4. https://doi.org/10.1128/mBio.00497-13.
Picioreanu, C., Blauert, F., Horn, H., Wagner, M., 2018. Determination of mechanical properties of biofilms by modelling the deformation measured using optical coherence tomography. Water Res. 145, 588–598. https://doi.org/10.1016/j.watres.2018.08.070.
Picologlou, B.F., Zelver, N., Characklis, W.G., 1980. Biofilm growth and hydraulic performance. J. Hydraul. Div. 106, 733–746.
Rupp, C.J., Fux, C.A., Stoodley, P., 2005. Viscoelasticity of Staphylococcus aureus biofilms in response to fluid shear allows resistance to detachment and facilitates rolling migration. Appl. Environ. Microbiol. 71, 2175–2178. https://doi.org/10.1128/AEM.71.4.2175-2178.2005.
Schindelin, J., Arganda-Carreras, I., Frise, E., Kaynig, V., Longair, M., Pietzsch, T., Preibisch, S., Rueden, C., Saalfeld, S., Schmid, B., Tinevez, J.Y., White, D.J., Hartenstein, V., Eliceiri, K., Tomancak, P., Cardona, A., 2012. Fiji: an open-source platform for biological-image analysis. Nat. Methods 97 9, 676–682. https://doi.org/10.1038/nmeth.2019, 2012.
Schultz, M.P., Bendick, J.A., Holm, E.R., Hertel, W.M., 2011. Economic impact of biofouling on a naval surface ship. Biofouling 27, 87–98. https://doi.org/10.1080/08927014.2010.542809.
Schultz, M.P., Swain, G.W., 2000. The influence of biofilms on skin friction drag. Biofouling 15, 129–139. https://doi.org/10.1080/08927010009386304.
Schultz, M.P., Walker, J.M., Steppe, C.N., Flack, K.A., 2015. Impact of diatomaceous biofilms on the frictional drag of fouling-release coatings. Biofouling 31, 759–773. https://doi.org/10.1080/08927014.2015.1108407.
Shanbhag, A.G., 1994. Utilization of information measure as a means of image thresholding. CVGIP Graph. Models Image Process. 56, 414–419. https://doi.org/10.1006/cgip.1994.1037.
Shaw, T., Winston, M., Rupp, C.J., Klapper, I., Stoodley, P., 2004. Commonality of elastic relaxation times in biofilms. Phys. Rev. Lett. 93, 1–4. https://doi.org/10.1103/PhysRevLett.93.098102.
Souza-Egipsy, V., Vega, J.F., González-Toril, E., Aguilera, Á., 2021. Biofilm mechanics in an extremely acidic environment: microbiological significance. Soft Matter 17, 3672. https://doi.org/10.1039/d0sm01975e.
Stewart, E.J., Ganesan, M., Younger, J.G., Solomon, M.J., 2015. Artificial biofilms establish the role of matrix interactions in staphylococcal biofilm assembly and disassembly. Sci. Rep. 5 https://doi.org/10.1038/srep13081.
Stoodley, P., Hall-Stoodley, L., Lappin-Scott, H.M., 2001. Detachment, surface migration, and other dynamic behavior in bacterial biofilms revealed by digital time-lapse imaging. Methods Enzymol. 337, 306–319. https://doi.org/10.1016/S0076-6879(01)37023-4.
Stoodley, P., Lewandowski, Z., Boyle, J.D., Lappin-Scott, H.M., 1999. Structural deformation of bacterial biofilms caused by short-term fluctuations in fluid shear: an in situ investigation of biofilm rheology. Biotechnol. Bioeng. 65, 83–92. https://doi.org/10.1002/(SICI)1097-0290(19991005)65:1<83::AID-BIT10>3.0.CO;2-B.
Strathmann, M., Griebe, T., Flemming, H.C., 2000. Artificial biofilm model- A useful tool for biofilm research. Appl. Microbiol. Biotechnol. 54, 231–237. https://doi.org/10.1007/s002530000370.
Team, R.C., 2019. R: A Language and Environment for Statistical Computing.
Titow, W.V., 1984. PVC technology. In: PVC Technology, fourth ed. Elsevier Applied Science Publishers. https://doi.org/10.1007/978-94-009-5614-8.
Townsin, R.L., 2003. The ship hull fouling penalty. Biofouling 19, 9–15. https://doi.org/10.1080/0892701031000088535.
Wagner, M., Horn, H., 2017. Optical coherence tomography in biofilm research: a comprehensive review. Biotechnol. Bioeng. 114, 1386–1402. https://doi.org/10.1002/bit.26283.
Wagner, M., Taherzadeh, D., Haisch, C., Horn, H., 2010. Investigation of the mesoscale structure and volumetric features of biofilms using optical coherence tomography. Biotechnol. Bioeng. 107, 844–853. https://doi.org/10.1002/bit.22864.
Watanabe, S., 1969. Augmentation in frictional resistance due to slime. J. Kansai Soc. Nav. Archit. 131, 45.
Werb, M., García, C.F., Bach, N.C., Grumbein, S., Sieber, S.A., Opitz, M., Lieleg, O., 2017. Surface topology affects wetting behavior of Bacillus subtilis biofilms. npj Biofilms Microbiomes 3. https://doi.org/10.1038/s41522-017-0018-1.
Xi, C., Marks, D., Schlachter, S., Luo, W., Boppart, S.A., 2006. High-resolution three-dimensional imaging of biofilm development using optical coherence tomography. J. Biomed. Opt. 11, 034001 https://doi.org/10.1117/1.2209962.
Yeginbayeva, I.A., Atlar, M., Turkmen, S., Chen, H., 2020. Biofouling Service' Conditions-Mimicked Hull Roughness Ranges and Biofilms-On the Surface and the Hydrodynamic Characteristics of Foul-Release Type Coatings. https://doi.org/10.1080/08927014.2020.1855330.
Yusim, A.K., Utama, I.K.A.P., 2017. An investigation into the drag increase on roughen surface due to marine fouling growth. IPTEK J. Technol. Sci. 28 https://doi.org/10.12962/J20882033.V28I3.3221.
Zou, G.X., Qu, J.P., Zou, X.L., 2007. Optimization of water absorption of starch/PVA composites. Polym. Compos. 28, 674–679. https://doi.org/10.1002/pc.20333.